47th AIAA Aerospace Sciences Meeting Including The New Horizons Forum and Aerospace Exposition
5 - 8 January 2009, Orlando, Florida

AIAA 2009-1270

Computational Modeling of Spanwise Flexibility Effects on Flapping Wing Aerodynamics

Hikaru Aono[1]*, Satish Kumar Chimakurthi[2]*, Carlos E. S. Cesnik[3]*, Hao Liu[4]**, and Wei Shyy[5]*

*University of Michigan, Ann Arbor, MI, 48109, U.S.A

**Chiba University, Chiba, Chiba, 263-8522, Japan

The implications of spanwise flexibility on flapping wing aerodynamics are investigated numerically for a rectangular wing in pure heave. A computational framework for fluid-structural interactions has been developed based on a direct coupling procedure between (i) a pressure-based finite-volume fluid flow solver based on the Navier-Stokes equations, and (ii) a quasi-3D finite element structural dynamics solver based on a geometrically nonlinear composite beam-like and linear plate-like formulations. The computational results are first correlated with available experimental data. It is shown that two key factors associated with spanwise wing deformation affect thrust generation, namely, in-phase motion between the wing tip and root, and the increased effective angle of attack of the deformed wing. If the wing motions resulting from both prescribed motion and deformation are correlated, the increased effective angle of attack at the tip could enhance the aerodynamic performance. If the flexibility is too high, then the wing tip and root could move in inconsistent directions, resulting in deteriorated aerodynamic performance.

Nomenclature

AR	=	aspect ratio = b^2/S
b	=	wing span
c	=	mean chord length (reference length)
C_L	=	lift coefficient $= F_v/(0.5\rho_f U_{ref}^2 S)$
C_T	=	thrust coefficient $= F_h/(0.5\rho_f U_{ref}^2 S)$
C_p	=	pressure coefficient $= p/(0.5\rho_f U_{ref}^2)$
D	=	flat plate bending stiffness $= Eh_w^3/12(1-\nu^2)$
E	=	Young's modulus of structure
f	=	plunging or flapping frequency
F_h	=	horizontal component of resultant aerodynamic force
F_v	=	vertical component of resultant aerodynamic force
h_a	=	flapping amplitude (e.g. amplitude of prescribed plunge motion)
h_{tip}	=	plunging or flapping amplitude at wing tip
h_{root}	=	plunging or flapping amplitude at wing root
h_w	=	thickness of flat plate
I_B	=	plunging or flapping moment of inertia
k	=	reduced frequency $= \omega c/(2U_{ref})$
p	=	static pressure

[1] Postdoctoral Research Fellow, Department of Aerospace Engineering, aonoh@umich.edu, Member AIAA.
[2] Doctoral Candidate, Department of Aerospace Engineering, satishkc@umich.edu, Member AIAA.
[3] Professor, Department of Aerospace Engineering, cesnik@umich.edu, Associate Fellow AIAA.
[4] Professor, Department of Engineering, hliu@faculty.chiba-u.jp, Member AIAA.
[5] Clarence L. "Kelly" Johnson Collegiate Professor and Chair, weishyy@umich.edu, Fellow AIAA.

$\bar{p}$ = non-dimensional positional component of fluid
Re = Reynolds number $= \rho_f U_{ref} c / \mu_f$
s = semi-span =b/2
St = Strouhal number $= \omega h_a / (\pi U_{ref})$
t = time
T = plunging or flapping period
u_i = i[th] velocity component of fluid
$\bar{u}_i$ = i[th] non-dimensional velocity component of fluid
U_{ref} = reference velocity (e.g. freestream velocity)
x, y, z = global Cartesian coordinate system
x_i = i[th] positional component of fluid
$\bar{x}_i$ = i[th] non-dimensional positional component of fluid
α_e = effective angle of attack of a wing at the wing tip $= \tan^{-1}\left(-\frac{1}{U_{ref}}\frac{dh_{tip}}{dt}\right)$
μ_f = dynamic viscosity of fluid
ν = Poisson ratio of structure
Π_1 = ratio of elastic and aerodynamic loadings $= D/(\rho_f U_{ref}^2 c^3)$
Π_2 = ratio of inertia and aerodynamic generalized forces $= I_B/(\rho_f c^5)$
Π_3 = ratio of the first bending mode to frequency of plunging or flapping of a wing $= \omega_B/\omega$
Π_4 = ratio of the second bending mode to frequency of plunging or flapping of a wing $= \omega_T/\omega$
ρ_f = density of fluid
ρ_s = density of structure
ω = circular frequency of flapping
ω_B = linear natural frequency of bending of a flapping wing
ω_T = linear natural frequency of torsion of a flapping wing
Ω_z = magnitude of spanwise (z) vorticity

I. Introduction

MICRO air vehicles (MAVs) are advancing our capabilities in the areas of environmental monitoring and homeland security[1]. MAVs have a maximum dimension on the order of 15 cm and nominal flight speeds of approximately 10 m/s, operating in a low Reynolds number (Re) regime (10^5 or lower). The rise and growth of MAVs have been stimulated by the long history of natural flight studies. Good reviews of the state-of-the-art in this subject are given in Refs. [2] and [3]. High-speed photography and stroboscopy indicate that most biological flyers undergo natural deformation in flight[4, 5]. Birds, bats, and insects exploit the coupling between flexible wings and aerodynamic forces such that the wing deformations improve aerodynamic performance[6]. Therefore, it is highly likely that, the interaction between unsteady aerodynamics and structural flexibility will be of considerable importance for MAV development[1].

Much of the aeroelasticity efforts thus far have focused on fixed wing membrane-based MAVs[7-11]. Shyy *et al.*[7] and Lian and Shyy[8] have successfully investigated fixed membrane wing aerodynamics with free stream based on both computation and experiment. Stanford *et al.*[9] developed a direct comparison of wing displacements, strains, and aerodynamic loads obtained via a novel experimental setup with those obtained numerically. In their work, they considered both pre- and post-stall angles of attack and the computed flow structures revealed several key aeroelastic effects: decreased tip vortex strength, pressure spikes and flow deceleration at the tangent discontinuity of the inflated membrane boundary, and an adaptive shift of pressure distribution in response to aerodynamic loading.

As to the studies of aeroelasticity of flexible flapping wing, Smith[12] first investigated numerically the effects of flexibility on the aerodynamics of single flapping moth wing by modeling it as a linear elastic structure for a Re of the order of 10^3 and reduced frequencies of the order of 0.2 and higher. In the structural modeling, the veins of the wings were treated as tubular beams of varying thickness, and the wing surfaces were modeled as quadrilateral (or triangular) membranes that are also of varying thickness with orthotropic properties using finite elements. For the

fluid dynamics model, an unsteady panel method was used with laminar flow assumption. Both the structural and the fluid equations were simultaneously solved to obtain the coupled flapping wing response. Frampton *et al.*[6] have studied a method of wing construction that results in an optimal relationship between flapping wing bending and twisting such that optimal thrust forces are generated. The thrust production of flexible flapping wings was tested in an experimental rig. The results from this study indicated that the phase between bending motion and torsional motion is critical for the production of thrust. It was noted that a wing with bending and torsional motion in phase creates the largest thrust whereas a wing with the torsional motion lagging the bending motion by 90 degrees results in the best efficiency. Hamamoto *et al.*[13] have investigated a deformable single wing of a dragonfly in hovering flight using arbitrary Lagrangina-Eulerian-based finite element method and examined the advantages and disadvantages of flexibility. They found that the flexible wing with nearly the same average energy consumption generated almost the same amount of lift force as the rigid wing with modified flapping motion. In this case, the motion of the tip of the flexible wing provided equivalent lift as the motion of the root of the rigid wing. However, the rigid wing required 19% more peak torque and 34% more peak power, indicating the usefulness of wing flexibility. Singh[14] developed a computational aeroelastic framework to support development of hover-capable, bio-inspired flapping wing vehicles. A finite element-based structural analysis of the wing was used along with an unsteady aerodynamic analysis based on indicial functions. The results suggested that at high flapping frequencies (~ 12 Hz), the light-weight and highly flexible insect-like wings used in the study (*Re*: 10^3-10^5) exhibited significant aeroelastic effects. Wills *et al.*[15] have presented a computational framework to design and analyze flapping MAV flight. A series of different geometric and physical fidelity level representations of solution methodologies was described in the work. Liani *et al.*[16] have investigated the aeroelastic effect on the aerodynamic forces produced by a flexible flapping wing at different frequencies especially near its resonance using coupling a two-dimensional unsteady panel method with Lagrange's equations of motion for a two degree-of-freedom (DOF) spring-mass wing section system. The results suggested that aerodynamic forces damp out elastic oscillations near the flutter boundaries which are a beneficial effect because it would allow the wing to vibrate close to the resonance frequency even if the structural damping is not considered.

The afore-described studies provide general insights into flexible wing aerodynamics. However, detailed analyses of the impact wing flexibility (both spanwise and chordwise) on flapping wing aerodynamics have not been presented enough in existing literature. Heathcote and Gursul[17] experimentally investigated the effect of chordwise flexibility of an airfoil in pure heave at low Reynolds numbers (*Re*: 10^3-10^4). The wake structures they visualized show a correspondingly stronger jet vortex pattern than that of rigid wing case and hence chordwise flexibility is found to bear efficiency benefits. Tang *et al.*[18] conducted numerical investigations based on the experimental models of Heathcote and Gursul[17]. They pointed out that the effect of the deformation (passive pitching) is similar to the rigid body motion (rigid pitching), meaning that the detailed shape of the airfoil is secondary to the equivalent angle of attack. On the other hand, Liu and Bose[19] investigated the effect of spanwise flexibility on the flukes of an immature fin whale using inviscid computations. They showed that phase of the flexing motion relative to the heave played a key role in determining thrust and efficiency characteristics of the fin. In particular, the in-phase motion of the wing tip was found to be beneficial in terms of increase in efficiency and the thrust. Recently, Heathcote *et al.*[20] experimentally investigated the effects of spanwise stiffness on thrust generation of rectangular wings undergoing a pure plunging motion under various free stream velocities (at *Re*: 10^4) in a water tunnel. Their direct force measurements suggested that the thrust/input-power ratio was found to be greater for flexible airfoils than for the rigid one. They also showed that at high plunging frequencies, the less flexible airfoil generates the largest thrust, while the more flexible airfoil generates the most thrust at low frequencies. They also observed that for Strouhal numbers greater than 0.2, a degree of spanwise flexibility was found to be beneficial. More recently, Chimakurthi *et al.*[21] performed numerical simulations following the experiment models of Heathcote *et al.* [20]. They suggested that spanwise flexibility could be more beneficial than a rigid wing for thrust generation. In addition, Zhu[22] investigated the effects of chord- and span-wise flexibility of flapping wing for a *Re* of 2.0×10^4 based on a combination of boundary-element method and a two-dimensional nonlinear thin-plate model. His results suggested that when the wing is immersed in air, the chordwise flexibility reduces both the thrust and the propulsion efficiency and the spanwise flexibility (through equivalent plunge and pitch flexibility) increases the thrust without efficiency reduction within a small range of structural parameters. While when the wing is immersed in water, the chordwise flexibility increased the efficiency and the spanwise flexibility reduced both the thrust and the efficiency. All the studies discussed thus far have described the effect of wing stiffness on flapping wing aerodynamics. However, few studies have investigated parametric variations to understand the impact of flexibility on aerodynamics, particularly regarding scaling laws.

Table 1. Dimensionless parameters and scaling dependency for flapping wing aerodynamics.

Dimensionless Parameter	***Hovering (no-freestream)*** <u>*Based on flapping wing velocity*</u>		***Forward Flight*** <u>*Based on cruising velocity*</u>	
	Length	***Frequency***	***Length***	***Frequency***
Reynolds number: $Re= U_{ref}c/\nu$	ℓ^2	f	ℓ	*Independent*
Strouhal number: $St=\omega h_a/(\pi U_{ref})$	*independent*	*independent*	ℓ	f
Reduced frequency: $k=\omega c/(2U_{ref})$	*independent*	*independent*	ℓ	f
$\Pi_1= D/(\rho_f U^2 c^3)$	ℓ^{-2}	f^{-2}	*independent*	*independent*
$\Pi_2= I_B/(\rho_f c^5)$	ℓ^{-1}	*independent*	ℓ^{-1}	*independent*
$\Pi_3= \omega_B/\omega$	ℓ^{-1}	f^{-1}	ℓ^{-1}	f^{-1}
$\Pi_4= \omega_T/\omega$	ℓ^{-1}	f^{-1}	ℓ^{-1}	f^{-1}

From the viewpoint of fluid and structural dynamics, there are different dimensionless parameters that are of relevance to flapping wing aerodynamics. Consider: c, chord length; ω, circular frequency of flapping (rad); h_a, flapping amplitude; U_{ref}, reference velocity; ν kinematic viscosity; ρ_f, fluid density; D, plate stiffness (directly proportional to material Young's modulus and the cube of the wing thickness); I_B, (flapping) moment of inertia; ω_B and ω_T being wing linear natural frequencies of bending and torsion respectively. The relevant dimensionless parameters are listed in Table 1[23]. Assuming that the geometric similarity is maintained, the scaling laws for forward and hovering flight conditions are summarized in the same table. One can readily conclude that the hovering Reynolds number and the cruising Reynolds number are very close to each other because the characteristic velocity for hovering is $U_{ref} = \omega h_a$. For hovering, the reduced frequency becomes $k=c/(2h_a)$, which is simply related to the normalized stroke amplitude. Furthermore, if the forward flight velocity is used as the velocity scale, then the resulting non-dimensional form of the momentum equation explicitly contains Reynolds number and Strouhal number. On the other hand, if the flapping wing velocity is chosen as the velocity scale, then the momentum equation will explicitly contain Reynolds number and reduced frequency[1]. As shown in Table 1, the scaling laws make the construction of aeroelastic models and testing complicated. For the calculation of the plate stiffness in Π_1, Young's modulus information along the span was considered. Also, it may be noted that, in the calculation of the dimensionless parameters Π_2, Π_3, and Π_4, the wing was assumed to be a beam with a rectangular cross-section whose length is equal to the mean chord and breadth to the mean thickness of the wing. These parametric and scaling laws have been introduced in fixed and rotary wing studies and the results suggested that they are very important and useful to model and analyze the aeroelastic problems[24, 25].

This paper is part of an ongoing study in the computational aeroelasticity of flapping wings. Previously, a computational aeroelasticity framework involving a Navier-Stokes solver and two different structural solvers of variable fidelity was introduced[21]. Validation studies with experiment were presented on a model example problem corresponding to a NACA0012 wing of aspect ratio 3 in pure heave motion at a Re of 3×10^4. In an attempt to continue the validation of the aeroelasticity framework and to obtain some more fundamental understanding of the impact of spanwise flexibility on flapping wing aerodynamics, several variations of spanwise flexibility of wing configurations were chosen. Further, keeping the bigger goal of simulating computational models of natural flyers with complex flapping kinematics[26] in mind, it was considered necessary to first understand the inertial/aeroelastic response of a wing prescribed with simplified motions. The main objectives of this paper are to: a) present studies on model a wing configuration (a flexible rectangular wing) prescribed with simplified kinematics (e.g. pure plunge); b) discuss the interplay between fluid and structural dynamics with reference to key parameters; and c) to examine the impact of spanwise flexibility on flapping wing aerodynamics and its sensitivity to phase lag between the prescribed motion and the dynamic response.

II. Numerical Framework for High-Fidelity Flapping Wing Simulations

In this section, a brief description of the fluid and structural dynamics approaches for the aeroelastic analysis of flapping wing is presented. From these, an aeroelastic framework is developed for the analysis of low *Re* flows and their interactions with flexible flapping wings.

A. Computational Fluid Dynamics Modeling (STREAM)

The fluid solution is obtained from the unsteady, incompressible 3D Navier-Stokes (NS) equations and the continuity equation where ρ_f is the fluid density, u_i is the velocity vector, t is the time, x_i is the position vector,

$$\begin{aligned} &\frac{\partial u_i}{\partial t} + \frac{\partial}{\partial x_j}(u_j u_i) = -\frac{1}{\rho_f}\frac{\partial p}{\partial x_i} + \frac{\mu_f}{\rho_f}\frac{\partial^2 u_i}{\partial x_j^2} \\ &\frac{\partial u_i}{\partial x_i} = 0 \end{aligned} \tag{1}$$

p is the pressure. If the reference velocity (U_{ref}), the chord length (c) and the inverse plunging/pitching ($1/f$) frequency are used as the velocity, length, and time scales respectively, Reynolds and Strouhal numbers are defined as, $Re = \rho_f U_{ref} c / \mu_f$ and $St = \omega h_a / (\pi U_{ref})$. With these choices of the scaling parameters, the non-dimensional form of the NS equations is written as:

$$St\frac{\partial}{\partial \bar{t}}(\bar{u}_i) + \frac{\partial}{\partial \bar{x}_j}(\bar{u}_j \bar{u}_i) = -\frac{\partial \bar{p}}{\partial \bar{x}_i} + \frac{1}{Re}\frac{\partial^2 \bar{u}_i}{\partial \bar{x}_j^2} \tag{2}$$

It should be noted that the relation between Strouhal number and the reduced frequency is $St = 2h_a k/(c\pi)$. The numerical solution is obtained using a pressure-based algorithm, with an employment of combined Cartesian and contravariant velocity variables to facilitate strong conservation law formulations and consistent finite-volume treatment. The convection terms are discretized using a second-order upwind scheme, while the pressure and viscous terms with a second-order central difference scheme. For the time integration, an implicit Euler scheme is employed. A moving grid technique employing the master-slave concept[8] is used to re-mesh the multi-block structured grid for fluid-structure interaction problems. The geometric conservation law (GCL) originally proposed by Thomas and Lombard[27] was incorporated to compute the cell volumes in the moving boundary problem consistently and eliminate artificial mass sources. The specific implementation and implications of the GCL in the context of the present solution algorithm have been discussed by Shyy *et al.*[28].

B. Computational Structural Dynamics Modeling (UM/NLABS)

The geometrically-nonlinear structural dynamic solution is based on an asymptotic approach to the equations governing the dynamics of a general 3D anisotropic slender solid[29, 30]. It is implemented in the University of Michigan's Nonlinear Active Beam Solver (UM/NLABS) computer code. Assuming the presence of a small parameter (the inverse of the wing aspect ratio) allows for a multi-scale solution process, in which the problem is decomposed into separate cross-sectional (small-scale) and longitudinal (long-scale) analyses. The longitudinal problem solves for average measures of deformation of the reference line under given external excitations. The cross-sectional problem solves the local deformation for given values of the long-scale variables. Both problems are tightly coupled and together provide an efficient approximation to the displacement field in the original 3D domain. A flow diagram of the process is shown in Figure 1.

The present implementation of this formulation follows the approach described in Ref. [31], where the solution to the structural dynamics problem is obtained by means of a finite-element discretization on a mixed-variational form of the equations. Although they are analyzed independently, the small and long-scale problems are intimately linked in the detailed approximation to the solution. This is particularly important in the generation of the solid side of an aeroelastic model: the interface of the structural model consists of the actual wetted surfaces of the vehicle, without extrapolations from the motion of a reduced-dimension structural model, nor the assumption of rigid cross sections typically found in beam theories.

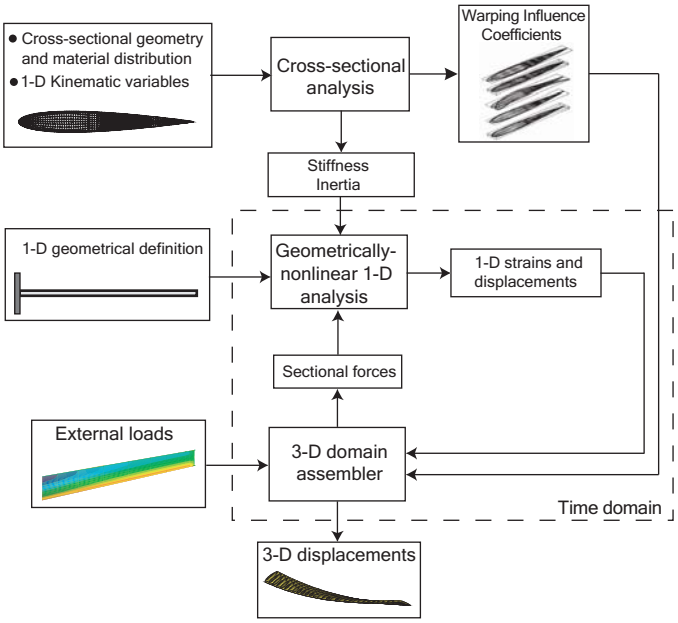

Figure 1. Asymptotic solution process for 3-D slender structures implemented in UM/NLABS.

C. Aeroelastic Coupling

The aeroelastic coupled solution is based on a time-domain partitioned solution process in which the nonlinear partial differential equations modeling the dynamic behavior of both fluid and structure are solved independently with boundary information (aerodynamic loads and structural displacements) being shared between each other alternately. A dedicated interface module was developed to enable communication between the flow and the structure at the 3D wetted surface (fluid-structure interface). In the interface module, both the fluid and the structural modules are called one after the other according to the coupling method adopted for the problem. The coupling algorithm is determined by the capability of the individual simulation code. For the cases where in-house structural solvers are involved, both explicit and implicit coupling methods are possible. More details of the coupling method amongst other things were presented in Ref. [21]

III. Models, Results, and Discussion

This section is divided into three subsections. In the first one, a brief description of the test problem that is considered in this study is provided. In the second subsection, details of the fluid and the structural computational models are provided. Finally, in the third subsection, computational results are presented for a rectangular wing configuration of NACA0012 cross-section in pure plunge and compared against experimental data from the studies of Heathcote *et al.*[20]. Further, the role of phase lag and the instantaneous effective angle of attack on the aerodynamic force generation is discussed.

A. Description of Test Case

The test-case studied is that of a spanwise-flexible rectangular wing (in forward flight) with root-prescribed plunge motion at the leading edge.

B. Computational and Experimental Models

Water tunnel studies have been performed on a flexible rectangular wing in pure heave by Heathcote *et al.*[20] to study the effect of spanwise flexibility on the thrust and the propulsive efficiency of this configuration. A schematic of the experimental set-up is shown in Figure 2 (a). As part of the experiment, three wing models of 0.3 m span and 0.1 m chord with varying levels of spanwise flexibility were constructed. The leading edge at the wing root was actuated by a prescribed sinusoidal plunge displacement profile as shown in Figure 3. Overall wing thrust coefficient

and vertical tip displacement response were experimentally measured. The representations of the cross-section constructions are reproduced in Figure 2 (b).

In the computation, a structured multi-block C-O type grid around a NACA0012 wing of aspect ratio 3 is used for the CFD simulations. The number of grid points is 120, 56, and 60 in the tangential, radial, and spanwise directions, respectively. Previously[21], grid refinement and time step sensitivity analyses have been performed to identify a suitable grid configuration in terms of the number of points, and the time step increment. The CFD model is shown in Figure 4 (a). For the boundary conditions at the inlet, the free-stream velocity (U_{ref}= 0.3 m/s) is prescribed and, for the outlet, the pressure gradient is set to zero. A no-slip condition on the flow velocity is assigned to the wing surface.

In this study, several wing structures of progressively increasing flexibility have been investigated. The results are compared with the experimental data of Heathcote *et al*. [20]. Furthermore, the velocity and pressure characteristics have been studied in detail while correlating with the dynamic wing motion. In the rigid wing case (corresponding to the "Inflexible" wing case in Heathcote *et al*.'s experiment[20]), the structure is considered to be infinitely stiff. For various flexible cases, Table 2 and Table 3 offer detailed property information. In all cases, a beam finite-element discretization with 39 elements along the semi-span was used. Chordwise deformation was reported as being negligible in the experiment[20], therefore, a beam model with six elastic degrees of freedom, corresponding to extension, twist, and shear and bending in two directions, was chosen. The beam reference line (cantilevered to a plunging frame of reference) is chosen along the leading edge of the wing (highlighted in red in Figure 4 (b)) and cross-sectional properties are evaluated with respect to the leading edge point. Furthermore, the properties are uniform throughout the semi-span. The contribution of the PDMS rubber material (used in the experimental wing configuration) to the overall mass and stiffness properties was found to be negligible; therefore, only the stainless steel ("Flexible-1(E= 210 GPa)"), the aluminium ("Flexible-2 (E= 70 GPa)"), and the "Flexible-3 (E= 40 GPa)" stiffeners (rectangular thin strip) were considered in the evaluation of cross-sectional properties (Figure 2 (b)). The latter does not correspond to any specific material and it has been created to better understand the experimental results obtained from the "Highly flexible" case. The 3D structural solution is obtained by using 75 recovery nodes on each cross section resulting in a structured grid of 3000 interface points which define the solid side of the aeroelastic interface. A summary of the geometrical and mechanical properties of a wing are included in Table 2. In Table 3, all dimensionless numbers related to either the structure, the flow, or to both are furnished. The dimensionless numbers Π_1, Π_2, Π_3 and Π_4 are discussed in more detail in Refs. [1] and [23].

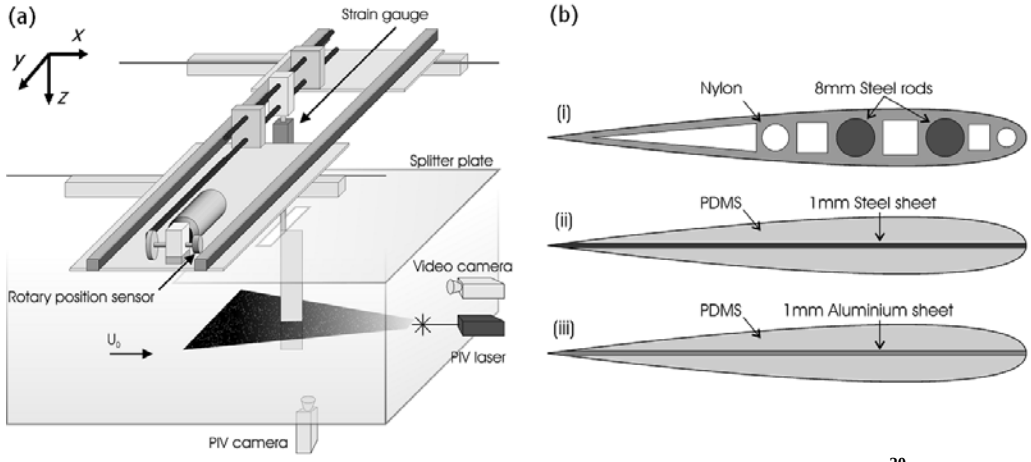

Figure 2. Experimental setup and wing cross-sections in Heathcote *et al.*'s experiment[20]. (a) Water-tunnel experiment setup; (b) Inflexible (i), Flexible (E= 210 GPa) (ii), Highly flexible (E= 70 GPa) (iii) wing cross-sections.

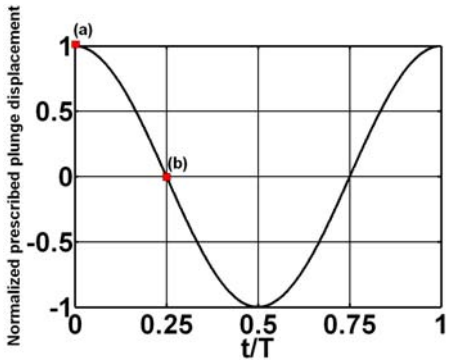

Figure 3. Prescribed plunge motion for the rectangular wing (normalized with respect to amplitude). Note that points (a) and (b) are representative time instants corresponding to 0 and T/4, respectively.

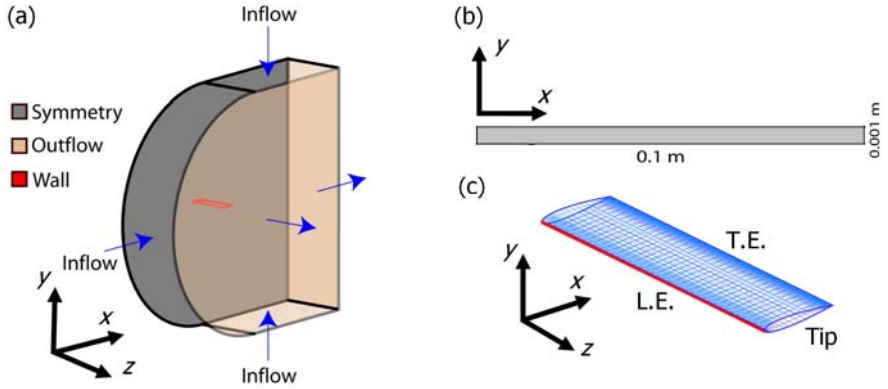

Figure 4. Computational model setup for the rectangular wing. (a) Computational model and boundary conditions for CFD (STREAM); (b) Computational model for CSD (UM/ULABS) (rectangular thin-strip cross section used to evaluate structural stiffness and mass properties); (c) The CSD-CFD interface grid with the beam reference line indicated with in red. Note that L.E. and T.E. indicate the leading and trailing edges of the wing, respectively.

Table 2. Geometric and mechanical properties of the wing models.

	'Flexible-1'	**'Flexible-2'**	**'Flexible-3'**
Semi-span [m]	3.0×10^{-1}	3.0×10^{-1}	3.0×10^{-1}
Chord length [m]	1.0×10^{-1}	1.0×10^{-1}	1.0×10^{-1}
Structural thickness [m]	1.0×10^{-3}	1.0×10^{-3}	1.0×10^{-3}
Material density [kg/m^3]	7.8×10^{3}	2.7×10^{3}	2.7×10^{3}
Young's modulus [Pa]	2.1×10^{11}	7.0×10^{10}	4.0×10^{10}

Table 3. Dimensionless parameters associated with wing models.

	'Flexible-1'	**'Flexible-2'**	**'Flexible-3'**
Chord-based Reynolds number: Re	3.0×10^{4}	3.0×10^{4}	3.0×10^{4}
Strouhal number: St	2.02×10^{-1}	2.02×10^{-1}	2.02×10^{-1}
Reduced frequency: k	1.82×10^{0}	1.82×10^{0}	1.82×10^{0}
Chord-normalized plunge amplitude: h_{root}	1.75×10^{-1}	1.75×10^{-1}	1.75×10^{-1}
Π_1	2.13×10^{2}	7.38×10^{1}	4.22×10^{1}
Π_2	7.80×10^{-1}	2.70×10^{-1}	2.70×10^{-1}
Π_3	5.46×10^{0}	5.18×10^{0}	5.18×10^{0}
Π_4	3.43×10^{1}	3.36×10^{1}	3.36×10^{1}

C. Results

In this study, special attention is given to the effect of spanwise flexibility in the case of Re= 3.0×10^4 and k= 1.82 in order to compare the computed results with available experimental data[20].

C.1 Deformation

Data corresponding to vertical displacement at the wing tip from the computation for "Rigid", "Flexible-1 (E= 210 GPa)", "Flexible-2 (E= 70 GPa)", and "Flexible-3 (E= 40 GPa)" wing cases and the experiment for "Inflexible", "Flexible", and "Highly flexible" are shown over one plunge cycle in Figure 5. Note that the displacement is normalized with respect to the amplitude of prescribed wing root movement (h_{root}). In the "Rigid" and "Flexible-1 (E= 210 GPa)" wing cases (Rigid (COMP) and Flexible-1 (COMP, E= 210 GPa) in Figure 5) the computed displacement responses show good agreement with the experiment data (Inflexible (EXP) and Flexible (EXP) in Figure 5) both qualitatively and quantitatively. However, slight discrepancy is observed in both amplitude and phase due to an uncertainty in both the computational models and experiments. More detailed comparisons of "Rigid" and 'Flexible-1' wing computational response with experimental data are presented in Ref. [21]. Further, following Figure 5, in the case of "Flexible-2 (COMP, E= 70 GPa)" wing, while the amplitude of computed displacement is considerably larger than that of the experiment (Highly flexible (EXP) in Figure 5), the phase lag at the tip is smaller by 27 deg. Note that the phase lag is measured with reference to the prescribed wing root movement. In addition, in the case of the "Flexible-3 (COMP, E= 40 GPa)" wing, the instantaneous structural response shows better match with the experimental data (Highly flexible (EXP) in Figure 5) than "Flexible-2 (COMP, E= 70 GPa)". In reality, several parameter variations were conducted to better understand the discrepancy between the experiment and the model for this particular case. The 43% drop in Young's modulus was found to provide the correct amount of flexibility encountered in the experimental results. It still remains to be seen if this is a reason for the observed discrepancy in deformation in the case of "Flexible-2 (COMP, E= 70 GPa)" wing. The normalized tip amplitude (h_{tip}/h_{root}) and phase lag angle (ϕ) information for all the cases are summarized in Table 4.

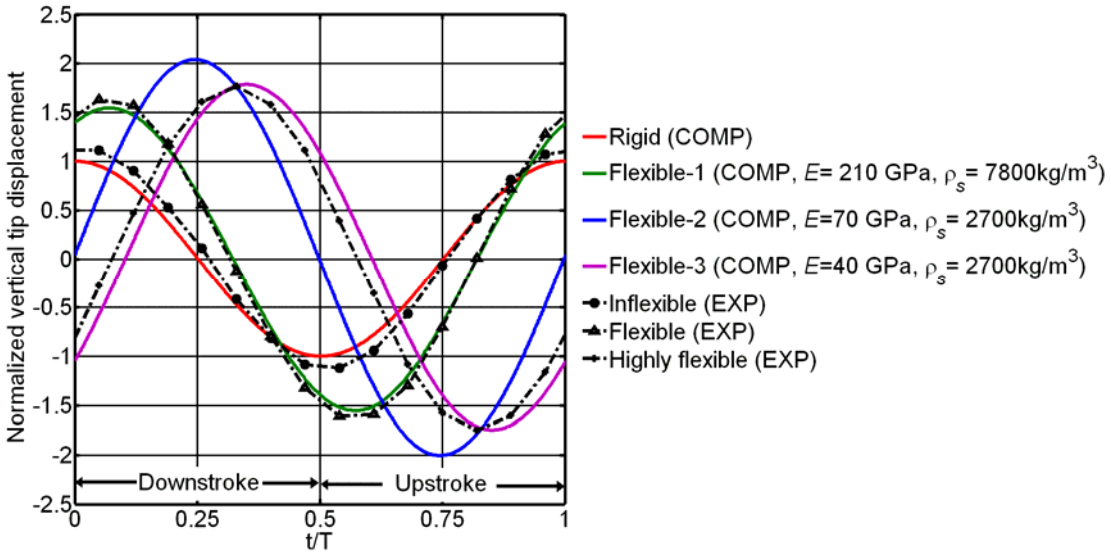

Figure 5. Comparison of experimental and computational vertical tip displacement for four variations of spanwise flexibility of the wing over a plunging cycle.

Table 4. Displacement and force data for the four computational wing models: Re= 3.0×10^4, k= 1.82

Wing model	h_{tip}/h_{root}	ϕ	$\bar{C}_T$
Rigid	1.0	0°	0.20
Flexible-1 (E= 210 GPa)	1.55	-25.7°	0.29
Flexible-2 (E= 70 GPa)	2.0	-90.0°	0.28
Flexible-3 (E= 40 GPa)	1.76	-126.3°	0.15

C.2 Flow Structures

Trailing-edge vortical structures from both the computation and the experiment are shown in Fig. 6 at two selected time instants (see Figure 3 (a) and (b)). For the "Rigid" and "Flexible-1 (E= 210 GPa)" wing cases, the computed tailing-edge vorticity contours at both time instants show an overall qualitatively good agreement with the experimental data in terms of location and rotational direction (see Figure 6(a) and (b)). However, some small scale vortices are not captured in the computed vortical structures. For the "Flexible-2 (E= 70 GPa)" wing case, at the beginning of downstroke (t/T = 0.0), the size of computed trailing-edge vortical structures is slightly larger than those of the experiment ((α-1, 2) and (β-1, 2) in Figure 6 (c)). Furthermore, a more fragmented vorticity pattern is seen in the experimental data. The computed wake structure near the wing tip is not the same as that of the experiment because of the difference in wing tip deflection. For the "Flexible-3 (E= 40 GPa)" wing case, at the beginning of downstroke, the computed trailing-edge vortical structures show overall agreement with those of the experiments ((α-1, 2) and (β-1, 2) in Figure 6 (d)). At the middle of downstroke (t/T = 0.25), i.e., at maximum plunging velocity of the wing root, in the computed results of the "Flexible-2 (E= 70 GPa)" wing case a counter-clockwise rotating vortex is seen near the trailing-edge ((α-3) and (α-4) in Figure 6 (c)). The "Flexible-3 (E= 40 GPa)" wing case and the experiments illustrate that a counter-clockwise rotating vortex is observed near the trailing-edge at mid semi-pan ((α-3) and (β-3) in Figure 6 (d)). The clockwise rotating trailing-edge vortex near the wing tip is shown in (α-4) and (β-4) in Figure 6 (d).

As shown in Figure 5, in the computed results of vertical displacement at the wing tip, for the "Flexible-2 (E= 70 GPa)" wing case, the wing tip in the computational model moves in the same direction as the root at the middle of downstroke, whereas it is opposite in the experiment. However, for the "Flexible-3 (E= 40 GPa)" wing case, the wing tip response is similar to that measured in the experiment. This discrepancy of the wing tip movement produces a visible different trailing-edge vortex structure mostly near the wing tip ((α-2, 4) and (β-2, 4) in Figure 6 (c)).

To gain better understanding of the impact of variation in material modulus to the flow patterns, flow structure and pressure (C_p) distributions around the wing for both the "Flexible-2 (E= 70 GPa) and Flexible-3 (E= 40 GPa)" wing cases at t/T of 0.25 are illustrated in Figure 7. The wing tip of the "Flexible-2 (E= 70 GPa)" wing case is in in-phase motion at this time instant, whereas the tip of the "Flexible-3 (E= 40 GPa)" wing case is in out-of-phase motion. Spanwise vorticity contours for the "Flexible-2 (E= 70 GPa)" wing case are shown in Figure 7 (1) at two different stations along the semi-span ('middle' and 'near the tip'). For this case, the contours near the mid semi-span show larger sized trailing-edge vortex than that seen in the "Flexible-3 (E= 40 GPa)" wing case. Further, a small leading-edge vortex (LEV) is observed on the lower surface whereas none is seen in the "Flexible-3 (E= 40 GPa)" wing case. At the section near the wing tip, in both the "Flexible-2 (E= 70 GPa) and Flexible-3 (E= 40 GPa)" wing cases a LEV is observed on the lower surface ((α-2) and (β-2) in Figure 7 (1)). Second, looking at Figure 7 (2) and (3), considerable differences may be found between both the computed results of flow field. In the normalized horizontal velocity contours of the "Flexible-2 (E= 70 GPa)" wing case, the area of accelerated flow is larger than that of the "Flexible-3 (E= 40 GPa)" wing case, especially near the trailing and leading edges, and the flow is separated near the leading edge of the lower surface. Although the normalized vertical velocity contours of the "Flexible-3 (E= 40 GPa)" wing case around the middle of the semi-span section show smaller area of induced flow than those of the "Flexible-2 (E= 70 GPa)" wing case, it is not the case near the wing tip. The flow features discussed so far correspond to pressure distribution on the wing surface and hence the aerodynamic force generation. Basically, the area of pressure curve of the "Flexible-2 (E= 70 GPa)" wing case is larger than that of the "Flexible-3 (E= 40 GPa)" wing case (Figure 7 (4)). Moreover, it is found that the acceleration and separation of flow near the trailing and leading edges are responsible for peak pressure on the wing surface. From the conservation law of momentum, the magnitude of velocity contours of the "Flexible-2 (E= 70 GPa)" wing case shows that it could produce larger aerodynamic forces than in the case of the "Flexible-3 (E= 40 GPa)" wing case.

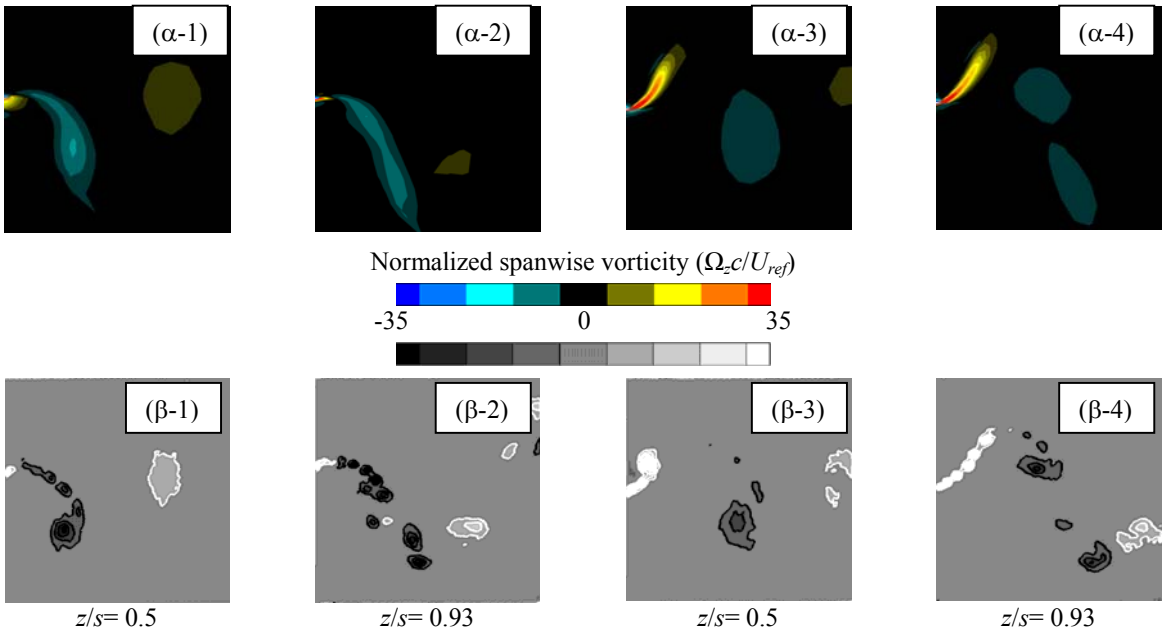

(a) Rigid, Upper: COMP, Lower: (*Inflexible*)

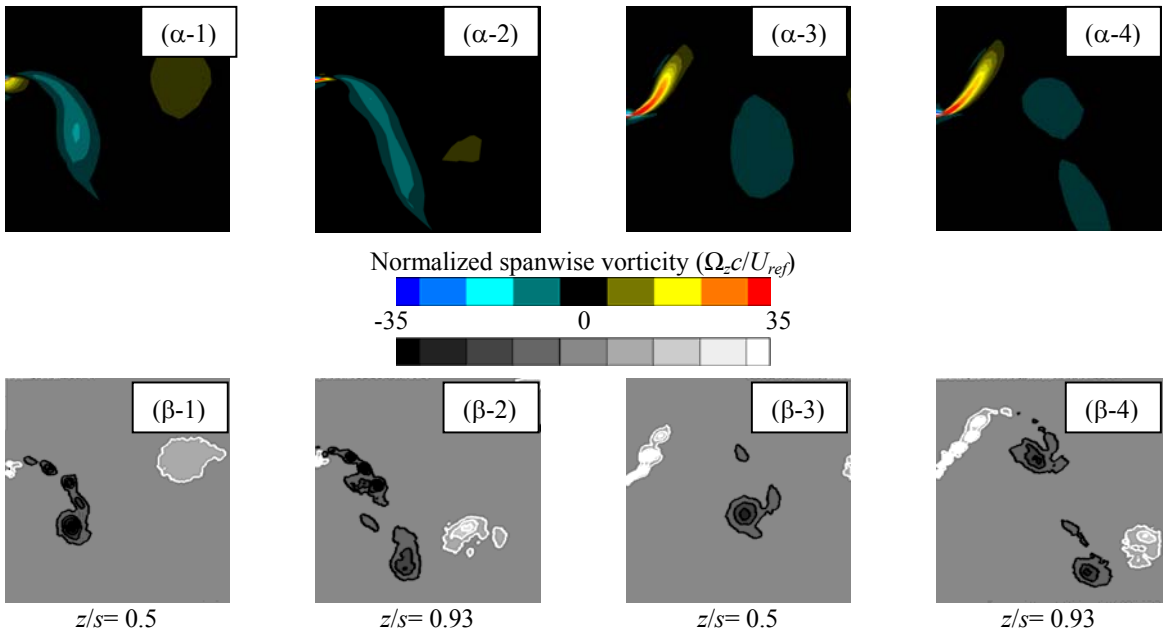

(b) Flexible-1, Upper: COMP (*E*= 210 GPa), Lower: EXP (*Flexible*)

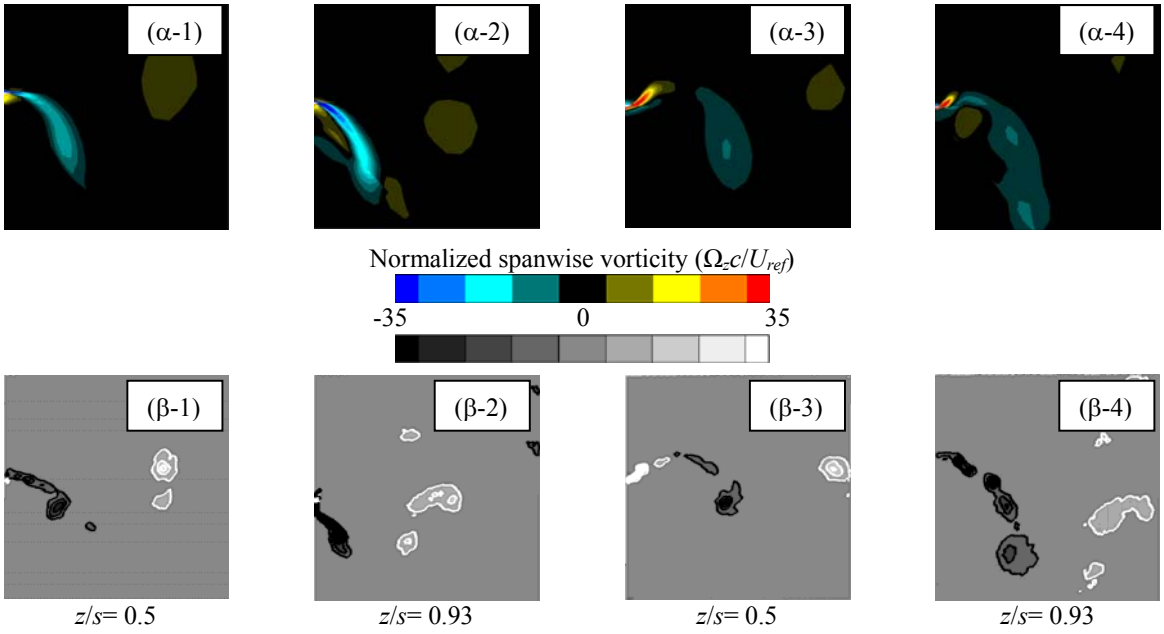

(c) Flexible-2, Upper: COMP (*E*= 70 GPa), Lower: EXP (*Highly Flexible*)

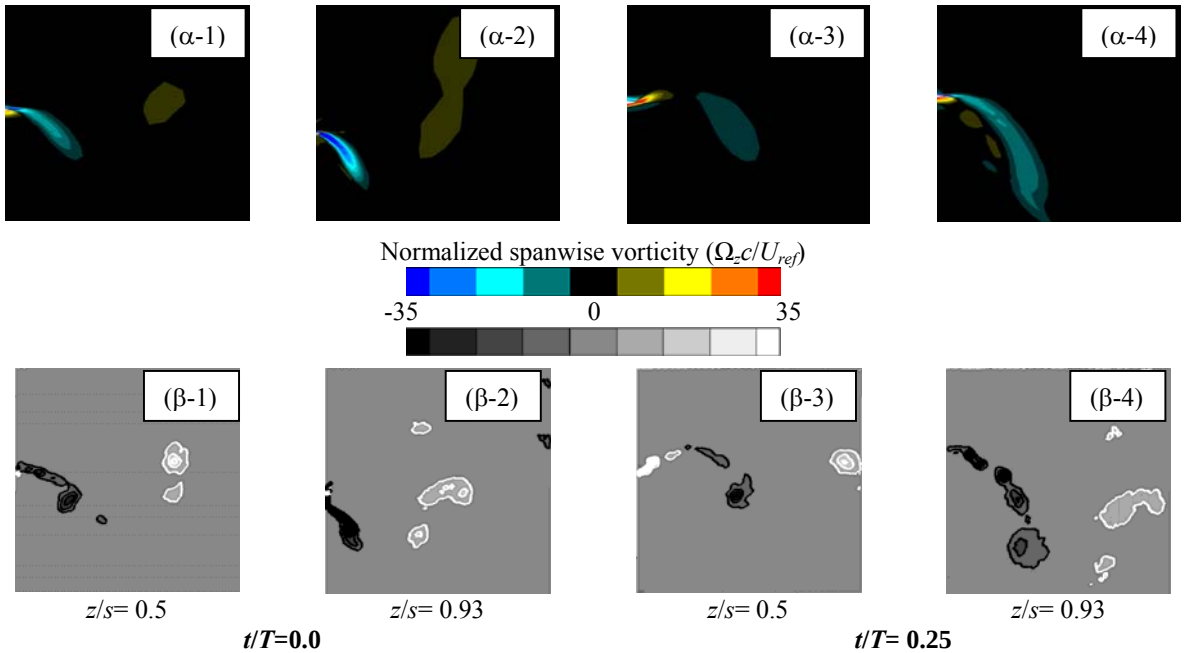

(d) Flexible-3, Upper: COMP (*E*= 40 GPa), Lower: EXP (*Highly Flexible*)

Figure 6. Spanwise-vortical structures around the trailing-edge at selected time instants. (a) Rigid; (b) Flexible-1 (*E*= 210 GPa); (c) Flexible-2 (*E*= 70 GPa); (d) Flexible-3 (*E*= 40 GPa). Note that spanwise vorticity is normalized by a factor of c/U_{ref}. The positive sign of spanwise vorticity indicates that the vortex rotation is in clock wise direction. Clockwise vorticity is shown in white in the experimental results[20] and red in the computational results, respectively.

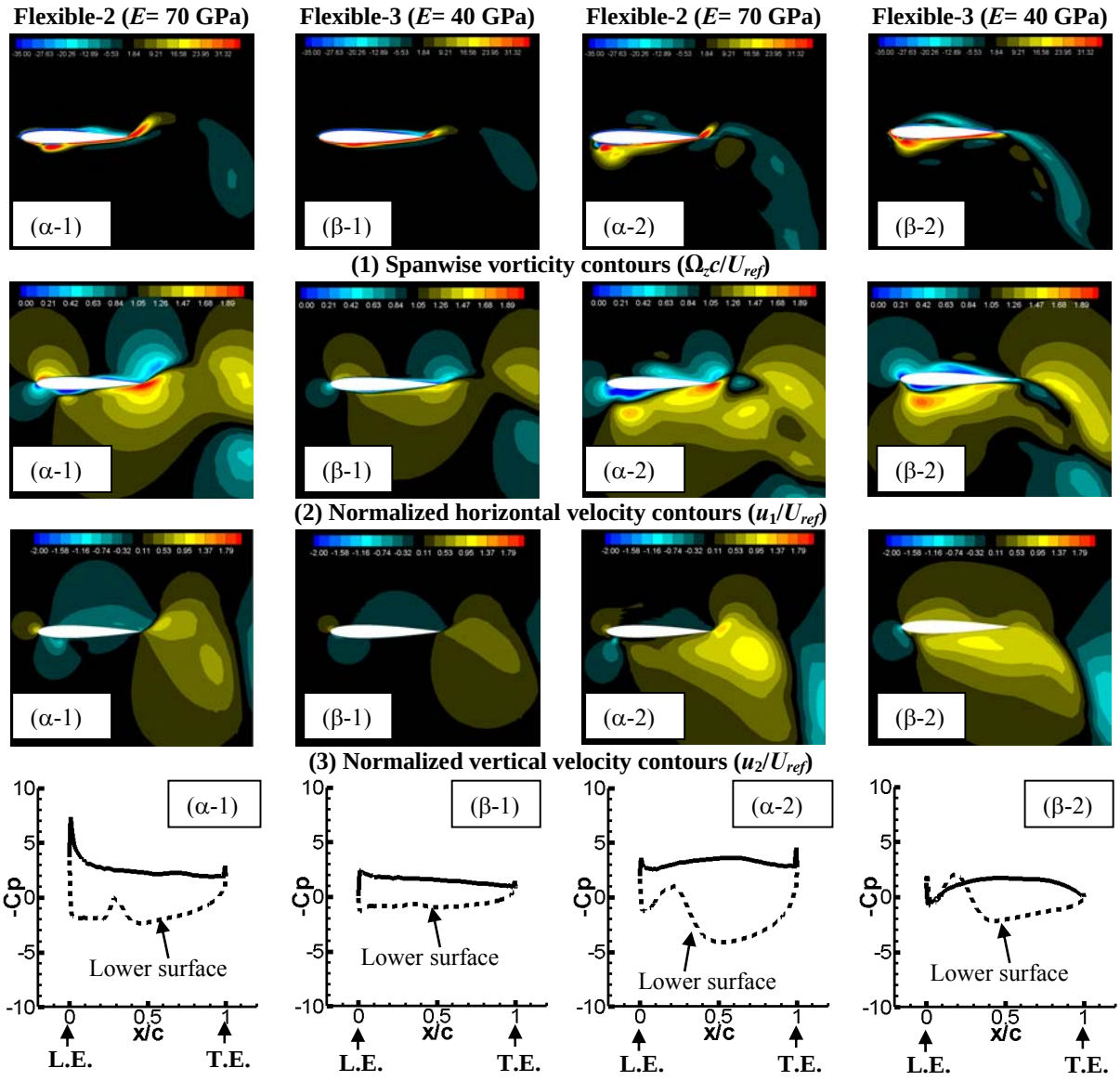

Figure 7. Comparison of computed results at *t*/*T* of 0.25 for the "Flexible-2 (*E*= 40 GPa)" and the "Flexible-3 (*E*= 70 GPa)" wing cases. (1) Spanwise vorticity contours; (2) Normalized horizontal velocity contours; (3) Normalized vertical velocity contours; (4) Pressure coefficient distributions. The results of two columns of left side are at the section of middle of semi-span and the others are near the wing tip. Note that velocity is normalized by inflow velocity (U_{ref}) and L.E. and T.E. indicate leading-and trailing-edge, respectively.

C.3 Aerodynamic forces

The time histories of thrust and lift coefficients for only the "Flexible-2 (*E*= 70 GPa)","Flexible-3 (*E*= 40 GPa)", and "Highly flexible (EXP)" wing cases are presented in Figure 8. The time response of thrust and lift coefficients in the "Flexible-3 (*E*= 40 GPa)" wing case shows a closer agreement with the experimental data ("Highly flexible") than that of the "Flexible-2 (*E*= 70 GPa)" wing case". One of the reasons for this is that the tip phase lag and vertical displacement amplitude of computation in the "Flexible-3 (*E*= 40 GPa)" wing case is much closer to the experiment than those computed in the "Flexible-2 (*E*= 70 GPa)" wing case (see Figure 5). According to the computed results of aerodynamic and structural responses, the "Flexible-3 (*E*= 40 GPa)" wing case is better than the "Flexible-2 (*E*= 70

GPa)" wing case in terms of correlation with experimental data. Therefore, the computed results of the "Flexible-3 (E= 40 GPa)" wing case are discussed further in the following section in order to investigate the effect of spanwise flexibility on plunging wing aerodynamics. However, the mean thrust coefficient for all the spanwise flexibility cases is presented in Table 4.

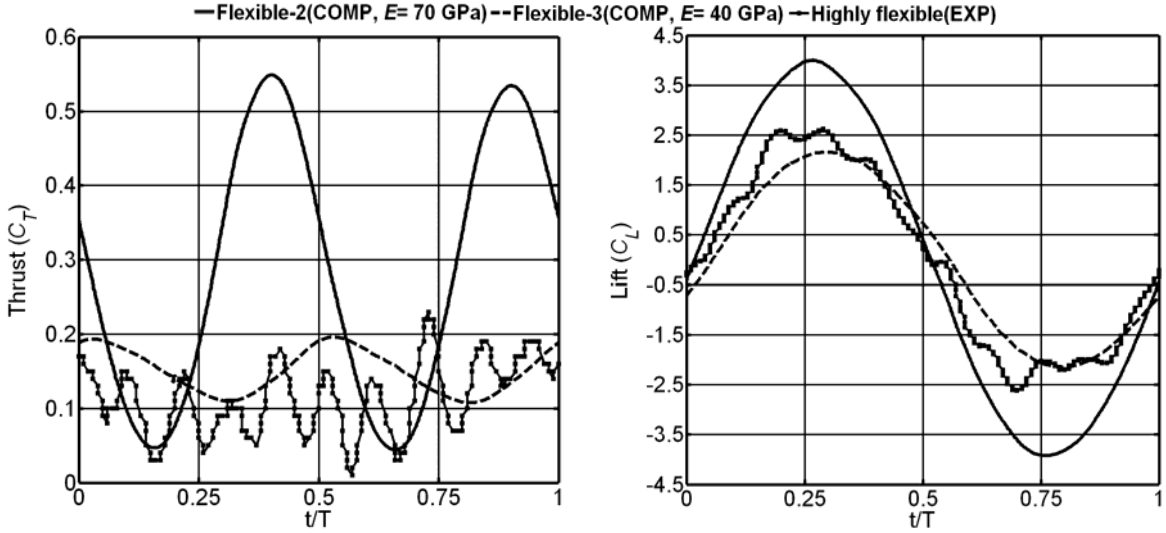

(A) Thrust coeffcieint **(B) Lift coefficient**

Figure 8. Effect of structural flexibility on instantaneous aerodynamic force generation. (A) Thrust; (b) Lift. Dashed and solid lines indicate the computed results corresponding to "Flexible-2 (E= 70 GPa)" and "Flexible-3 (E= 40 GPa)"wing cases, respectively. Solid line with square indicates the experimental results[20].

C.4 Role of phase motion of wing tip and instantaneous effective angle of attack (Re=3.0×10^4 and k= 1.82)

Focusing on the "Rigid", "Flexible-1 (E= 210 GPa)", and "Flexible-3 (E= 40 GPa)" wing cases, the role of phase lag and instantaneous effective angle of attack in the aerodynamic force generation is discussed.

Figure 9 shows the time histories of computed thrust coefficient and effective angle of attack at the wing tip for three variations of spanwise flexibility (i.e., "Rigid", "Flexible-1 (E= 210 GPa)", "Flexible-3 (E= 40 GPa)"). The blue block areas in Figure 9 indicate the out-of-phase motion of the wing tip. The blue blocks in the figures labeled as (A) show the 'out-of-phase' motion for the "Flexible-1 (E= 210 GPa)" wing case and the ones labeled as (B) show 'out-of-phase' motion for the "Flexible-3 (E= 40 GPa)" wing case. From the plots of thrust coefficient, it is clear that the "Flexible-1 (E= 210 GPa)" wing model produces higher peaks of thrust than that of "Rigid" wing and the "Flexible-3 (E= 40 GPa)" wing model generates smaller peaks of thrust than that of that of "Rigid" wing model. Focusing on the instantaneous effective angle of attack at the wing tip, for "Rigid" wing case, the instantaneous effective angle of attack is identical throughout the wing semi-span since there is no wing deformation. The time variation of the effective angle of attack forms a sinusoidal curve. For the "Flexible-1 (E= 210 GPa)" wing case, medium spanwise flexibility produces phase delay and increase of vertical displacement at the wing tip and hence the instantaneous effective angle of attack at the tip also has a small phase delay and appearance of larger effective angle of attack at the tip than that of rigid wing ((2) in Figure 9 (A)). For the "Flexible-3 (E= 40 GPa)" wing case, high spanwise flexibility creates large phase delay and increase of vertical displacement at the wing tip and hence instantaneous effective angle of attack at the tip has large phase delay and shows the largest effective angles of attack at the tip among all three cases ((2) in Figure 9 (B)). Focusing on the relationship between phase of the wing tip and the maximum effective angle of attack at the tip, for "Flexible-1(E= 210 GPa)" wing case, the maximum effective angle of attack at the tip is observed in in-phase motion of wing tip. On the other hand, for "Flexible-3 (E= 40 GPa)" wing case, maximum effective angle of attack at the tip is observed in the out-of-phase motion of the wing tip. Recalling the computed results of instantaneous thrust force generation, "Flexible-1 (E= 210 GPa)" wing case shows the best aerodynamic performance and not "Flexible-3 (E= 40 GPa)." According to these observations, two key parameters have been determined to improve aerodynamic performance due to spanwise flexibility of the wing undergoing pure plunge. One is higher effective angle of attack at the wing tip, and the other is 'in-phase motion' of the wing tip. For example, since the peak effective angle of attack at the wing tip in "Flexible-3 (E= 40 GPa)" wing case is observed during the out-of-phase motion, this case could not show an enhancement in the aerodynamic

performance with respect to the rigid one due to spanwise flexibility. The mean thrust coefficient as a function of spanwise flexibility is plotted in Figure 10 in which a nonlinear trend is clearly seen.

(A) Flexible-1 (*E*= 210 GPa)

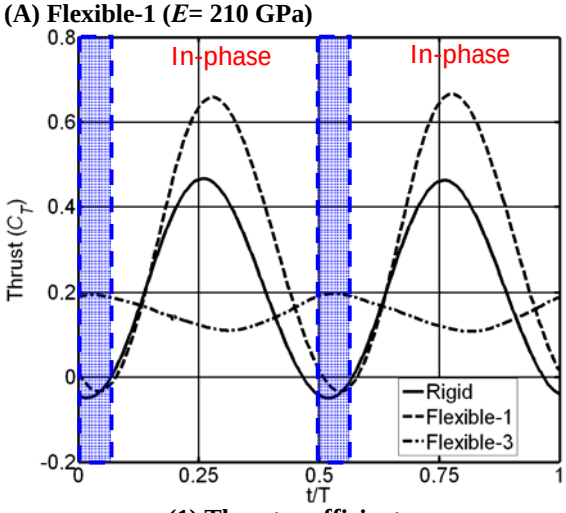

(1) Thrust coefficient

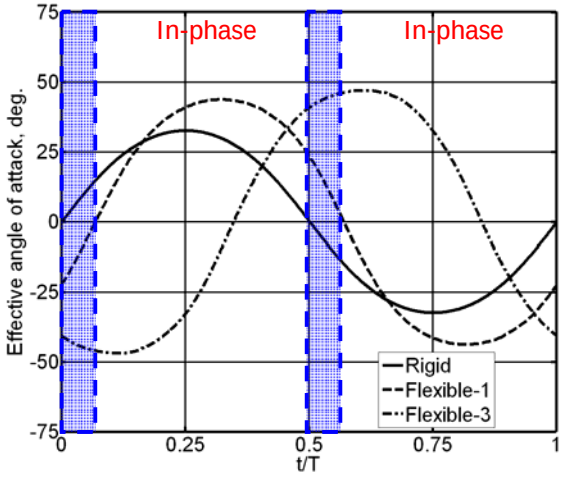

(2) Effective angle of attack at the wing tip

(B) Flexible-3 (*E*=40 GPa)

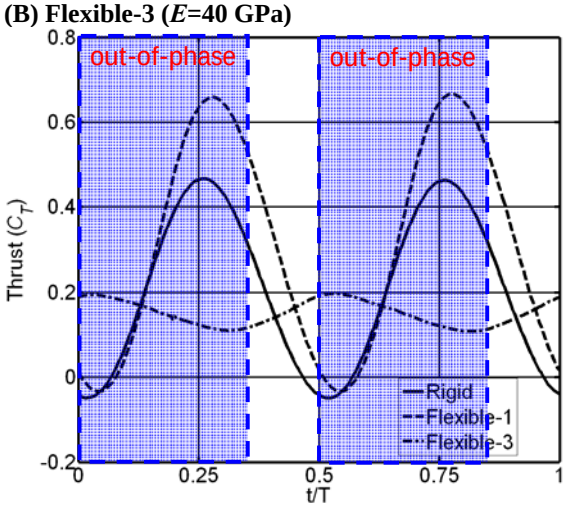

(1) Thrust coefficient

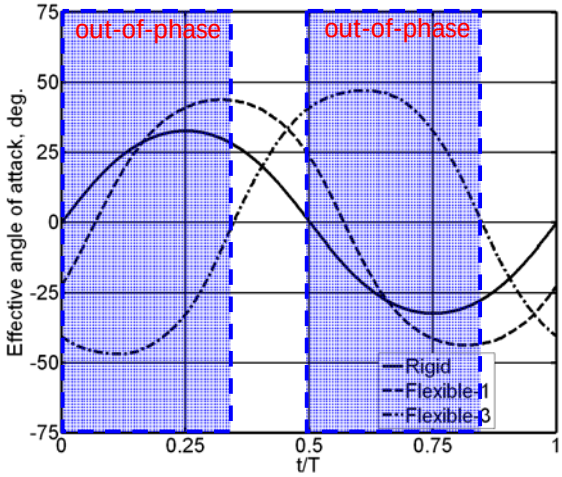

(2) Effective angle of attack at the wing tip

Figure 9. Time histories of thrust coefficient and effective angle of attack at the wing tip during one stroke. Solid, broken, and dot-dashed lines indicate the computed results of the "Rigid", the "Flexible-1 (*E*= 210 GPa)", and the "Flexible-3 (*E*= 40 GPa)", respectively. Note that blue blocked area represents that the wing tip is in out-of-phase motion.

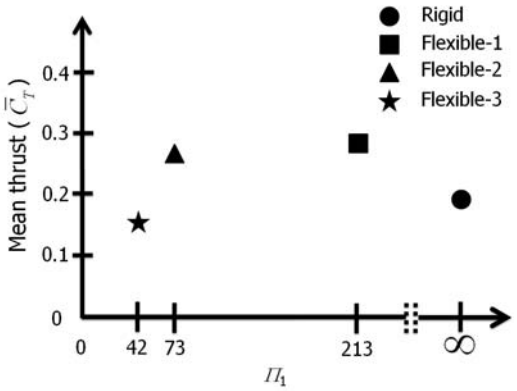

Figure 10. Mean thrust coefficient versus spanwise flexibility of the wing.

IV. Concluding Remarks

The impact of spanwise flexibility on flapping wing aerodynamics has been investigated numerically for a rectangular wing undergoing pure plunge. The wing cross section is the NACA 0012 airfoil, with an aspect ratio of 3, at a chord-based Reynolds number of 3×10^4 and reduced frequency of 1.82. The computational investigation is complemented by recently published experiments in Heathcote *et al.*[20]. To perform the analyses, a computational aeroelasticity framework has been developed based on a direct coupling procedure between (i) a finite-volume Navier-Stokes fluid dynamics solver, and (ii) a quasi-3D finite-element structural dynamic solver based on geometrically nonlinear composite beam-like and linear plate-like deformations. Quantitatively good agreement with available experimental data is obtained for instantaneous vertical tip displacement and thrust force on the flexible wing. Furthermore, qualitatively good agreement has been obtained for the flow structures including instantaneous spanwise vorticity characteristics.

Several key conclusions stem from the present study and are highlighted as follows:

1) Within a suitably selected range of spanwise flexibility, both mean and instantaneous thrust forces of a plunging wing could be enhanced due to wing deformation.

2) Phase lag of the wing tip response with respect to the prescribed motion is a critical factor for thrust generation. For instance, when the phase lag at the wing tip is less than 90 deg, spanwise flexibility is shown to have a favorable impact on the thrust generation.

3) Increased effective angle of attack at the wing tip is shown to be a secondary factor in the increase of thrust forces.

4) The highest mean thrust force is shown to have occurred when two conditions have been simultaneously satisfied: in-phase motion of the wing and an increased effective angle of attack at the tip. On the other hand, even when the effective angle of attack at the tip is increased, thrust forces are shown to have decreased when the wing motion at the tip is out-of-phase with respect to the root and hence a lower mean thrust is seen by the wing in this case.

Future work will address the combined plunge/pitch excitation of flapping wings with complex planform geometry and sectional profile.

Acknowledgments

The authors would like to thank Prof. Ismet Gursul and Mr. Sam Heathcote (University of Bath, U.K.) for providing experimental data for the rectangular wing case. This work was supported by the Air Force Office of Scientific Research's Multidisciplinary University Research Initiative (MURI) grant and by the Michigan/AFRL (Air Force Research Laboratory)/Boeing Collaborative Center in Aeronautical Sciences.

References

[1]Shyy, W., Lian, Y., Tang, J. Viieru, D. and Liu, H., *Aerodynamics of Low Reynolds Number Flyers*, Cambridge University Press, New York, 2008.

[2]Pines, D. J. and Bohorquez, F., "Challenges Facing Future Micro Air Vehicle Development," *Journal of Aircraft*, Vol. 43, No. 2, March-April 2006, pp. 290-305.

[3]Mueller, T. J.(ed.), *Fixed and Flapping Wing Aerodynamics for Micro Air Vehicle Applications*, Vol. 195, Progress in Astronautics and Aeronautics, AIAA, New York, 2001.

[4]Wootton, J., "Support and Deformability in Insect wings," *Journal of Zoology,* Vol. 193, 1981, pp. 447-468.

[5]Simon, M., W., Adrian L. R. T., and Graham K. T., "Photogrammetric Reconstruction of High-resolution Surface Topographies and Deformable Wing Kinematics of Tethered Locusts and Free-flying Hoverflies," *Journal of The Royal Society Interface,* DOI:10.1098/rsif.2008.0245

[6]Frampton, K. D., Goldfarb, M., Monopoli, D., and Cveticanin, D., "Passive Aeroelastic Tailoring for Optimal Flapping Wings," *Fixed and Flapping Wing Aerodynamics for Micro Air Vehicle Applications*, edited by T. J. Mueller, Vol. 195, Progress in Astronautics and Aeronautics, AIAA, New York, 2001, pp.473-482.

[7]Shyy, W., Ifju, P., and Viieru, D., "Membrane Wing-Based Micro Air Vehicles", *Applied Mechanics Reviews*, Vol. 58, No. 1-6, July 2005, pp. 283-301.

[8]Lian, Y. and Shyy, W., "Numerical Simulations of Membrane Wing Aerodynamics for Micro Air Vehicle Applications," *Journal of Aircraft*, Vol. 42, No. 4, 2005, pp. 865-873.

[9]Stanford, B., Sytsma, M., Albertani, R., Viieru, D., Shyy, W., and Ifju, P., "Static Aeroelastic Model Validation of Membrane Micro Air Vehicle Wings," *AIAA Journal*, Vol. 45, No. 12, Dec. 2007, pp. 2828-2837.

[10]Stults, J. A., Maple, R. C., Cobb, R. G., and Parker, G. H., "Computational Aeroelastic Analysis of a Micro Air Vehicle With Experimentally Determined modes," *23rd AIAA Applied Aerodynamics Conference*, Toronto, Ontario, Canada, June 6-9, 2005, AIAA Paper 2005-4614.

[11]Song, A., Tian, X., Israeli, E., Galvo, R., Bishop, K., Swartz, S., and Breuer, K., "The Aero-Mechanics of Low Aspect Ratio Compliant Membrane Wings, with Applications to Animal Flight," *46th AIAA Aerospace Sciences Meeting and Exhibit*, Reno, Nevada, 2008, AIAA Paper 2008-517.

[12]Smith, M. J. C., "The Effects of Flexibility on the Aerodynamics of Moth Wings: Towards the Development of Flapping-Wing Technology," *33rd Aerospace Sciences Meeting and Exhibit*, Reno, Nevada, 1995, AIAA Paper 95-0743.

[13]Hamamoto, M., Ohta, Y., Hara, K., and Hisada, T., "Application of Fluid-Structure Interaction Analysis to Flapping Flight of Insects With Deformable Wings, *Advanced Robotics*, Vol. 21, No. 1-2, 2007, pp. 1-21.

[14]Singh, B., "Dynamics and Aeroelasticity of Hover Capable Flapping Wings: Experiments and Analysis", Ph.D. Dissertation, Department of Aerospace Engineering, University of Maryland, College Park, Maryland, 2006.

[15]Wills, D., Israeli, E., Persson, P., Drela, M., Peraire, J., Swartz, S. M., and Breuer, K. S., "A Computational Framework for Fluid Structure Interaction in Biologically Inspired Flapping Flight," *25th AIAA Applied Aerodynamics Conference*, Miami, Florida, June 25-28, 2007, AIAA Paper 2007-3803.

[16]Liani, E., Guo, S., and Allegri, G., "Aeroelastic Effect on Flapping Wing Performance," *48th AIAA/ASME/ASCE/AHS/ASC Structures, Structural Dynamics, and Materials Conference*, Honololu, Hawaii, April, 2007, AIAA Paper 2007-2412.

[17]Heathcote, S., and Gursul, I., "Flexible flapping airfoil propulsion at low Reynolds numbers" *AIAA Journal*, Vol. 45, No. 5, 2007, pp. 1066-1079.

[18]Tang, J., Viieru, D., and Shyy, W., "A Study of Aerodynamics of Low Reynolds Number Flexible Airfoils," *37th AIAA Fluid Dynamics Conference and Exhibit*, Miami, Florida, June 2007, AIAA Paper 2007-4212.

[19]Liu, P., and Bose, N., "Propulsive Performance from Oscillating Propulsors with Spanwise Flexibility," *Proceedings: Mathematical, Physical and Engineering Sciences*, 1997, Vol.453, pp.1763-1770.

[20]Heathcote, S., Wang Z., and Gursul, I., "Effect of Spanwise Flexibility on Flapping Wing Propulsion," *Journal of Fluids and Structures*, Vol. 24, No. 2, 2008, pp. 183-199.

[21]Chimakurthi, S., K., Tang, J., Palacios, R., Cesnik C., E., S., and Shyy, W., "Computational Aeroelasticity Framework for Analyzing Flapping Wing Micro Air Vehicles," *49th*AIAA/ASME/ASCE/AHS/ASC Structures, Structural Dynamics, and Materials Conference, Schaumburg, Illinois, April. 2008, AIAA Paper 2008-1814.

[22]Zhu, Q., "Numerical Simulation of a Flapping Foil with Chordwise or Spanwise Flexibility," *AIAA Journal*, Vol. 45, No. 10, Oct. 2007, pp. 2448-2457.

[23]Shyy, W., Lian, Y., Tang, J., Liu, H., Trizila P., Stanford B., Bernal L., Cesnik, C.E.S., Friedmann, P., and Ifju, P., "Computational Aerodynamics of Low Reynolds Number Plunging, Pitching and Flexible Wings for MAV Applications," *Acta Mechanica Sinica*, Vol. 24, (2008), pp. 351-373; also, *46th AIAA Aerospace Sciences Meeting and Exhibit*, Reno, Nevada, Jan. 2008, AIAA Paper 2008-523.

[24]Fung, Y., C., *An Introduction to the theory of aeroelasticity*, Dover Publications, Inc. Mineola, New York, 1969.

[25]Friedmann, P., P., "Aeroelastic Scaling for Rotary-wing Aircraft with Application," *Journal of Fluids and Structures*, 2004, Vol. 19, pp. 635-650. DOI:10.1016/j.jfluidstructs.2004.03.003

[26]Fry, S., N., Sayaman, R., and Dickinson, M. H., "The Aerodynamics of Free-Flight Maneuvers in *Drosophila*," *Science*, 2003, Vol. 300, No. 5618, pp. 495-498. DOI: 10.1126/science.1081944

[27]Thomas, P. D. and Lombard, K., "Geometric Conservation Law and its Application to Flow Computations on Moving Grids," *AIAA Journal*, Vol. 17, No. 10, 1979, pp. 1030-1037.

[28]Shyy, W., Udaykumar, H. S., Rao, M. M., and Smith, R. W., *Computational Fluid Dynamics with Moving Boundaries*, Dover, New York, 2007.
[29]Palacios, R. and Cesnik, C. E. S., "A Geometrically Nonlinear Theory of Active Composite Beams with Deformable Cross-Sections," *AIAA Journal*, Vol. 46, No. 2, 2008, pp. 439-450.
[30]Palacios, R. and Cesnik, C. E. S., "Cross-Sectional Analysis of Non-homogenous Anisotropic Active Slender Structures," *AIAA Journal*, Vol. 43, No.12, 2005, pp. 2624-2638.
[31]Cesnik C. E. S. and Hodges D. H., "VABS: A New Concept for Composite Rotor Blade Cross-Sectional Modeling," *Journal of the American Helicopter Society*, Vol. 42, No. 1, Jan. 1997, pp. 27-38.